ACS APPLIED MATERIALS & INTERFACES

Research Article

www.acsami.org

Extensive Penetration of Evaporated Electrode Metals into Fullerene Films: Intercalated Metal Nanostructures and Influence on Device Architecture

Guangye Zhang,[†] Steven A. Hawks,[‡] Chilan Ngo,[‡] Laura T. Schelhas,[†] D. Tyler Scholes,[†] Hyeyeon Kang,[†] Jordan C. Aguirre,[†] Sarah H. Tolbert,[†,‡,§] and Benjamin J. Schwartz*[,†,§]

[†]Department of Chemistry and Biochemistry, University of California, Los Angeles, Los Angeles, California 90095-1569, United States

[‡]Department of Materials Science and Engineering, University of California, Los Angeles, Los Angeles, California 90095, United States

[§]California NanoSystems Institute, University of California, Los Angeles, Los Angeles, California 90095, United States

Supporting Information

ABSTRACT: Although it is known that evaporated metals can penetrate into films of various organic molecules that are a few nanometers thick, there has been little work aimed at exploring the interaction of the common electrode metals used in devices with fullerene derivatives, such as organic photovoltaics (OPVs) or perovskite solar cells that use fullerenes as electron transport layers. In this paper, we show that when commonly used electrode metals (e.g., Au, Ag, Al, Ca, etc.) are evaporated onto films of fullerene derivatives (such as [6,6]-phenyl-C_{61}-butyric acid methyl ester (PCBM)), the metal penetrates many tens of nanometers into the fullerene layer. This penetration decreases the effective electrical thickness of fullerene-based sandwich structure devices, as measured by the device's geometric capacitance, and thus significantly alters the device physics. For the case of Au/PCBM, the metal penetrates a remarkable 70 nm into the fullerene, and we see penetration of similar magnitude in a wide variety of fullerene derivative/evaporated metal combinations. Moreover, using transmission electron microscopy to observed cross-sections of the films, we show that when gold is evaporated onto poly(3-hexylthiophene) (P3HT)/PCBM sequentially processed OPV quasi-bilayers, Au nanoparticles with diameters of ∼3−20 nm are formed and are dispersed entirely throughout the fullerene-rich overlayer. The plasmonic absorption and scattering from these nanoparticles are readily evident in the optical transmission spectrum, demonstrating that the interpenetrated metal significantly alters the optical properties of fullerene-rich active layers. This opens a number of possibilities in terms of contact engineering and light management so that metal penetration in devices that use fullerene derivatives could be used to advantage, making it critical that researchers are aware of the electronic and optical consequences of exposing fullerene-derivative films to evaporated electrode metals.

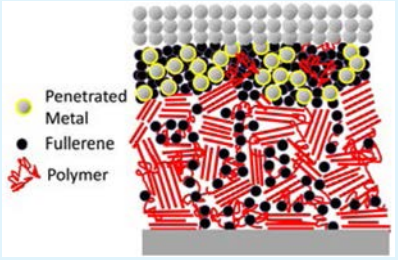

KEYWORDS: *fullerene, PCBM, sequential processing, metal penetration, organic photovoltaic, conjugated polymer, gold nanoparticles, plasmonics*

1. INTRODUCTION

Polymer:fullerene bulk heterojunction (BHJ) organic photovoltaics (OPVs)[1,2] and perovskite-based solar cells[3,4] have attracted widespread interest as potential low-cost solar energy harvesters. Although much research has been directed toward the optoelectronic processes occurring within the cell's photoactive layer,[5−10] another critically important aspect of these devices is their mesoscopic structure. In OPVs, for example, it is desirable to have a vertical composition profile that is enriched in fullerene material at the electron-collecting contact to promote charge extraction out of the active layer and increase cathode selectivity.[11−14] Perovskite-based solar cells also often use fullerene electron transport layers between the active layer and the cathode for the same reason.[15−17] For both types of devices, the correct energetic alignment and conductivity are important for achieving, as closely as possible, selective Ohmic contacts.[15,17−20]

Despite a significant amount of research on both OPVs and perovskite-based solar cells, somewhat less attention has been paid to the morphology of the electrode interfaces.[21,22] It is typically assumed that the deposition techniques (e.g., thermal evaporation, spin coating, etc.) used to create the device give clean interfaces with minimal ($\lesssim$ a few nanometers) interpenetration.[21] In particular, there is little work examining how commonly used evaporated cathode metals, such as Ca or Al, specifically interact with the fullerene component of the active

Received: August 3, 2015
Accepted: October 21, 2015
Published: October 21, 2015

DOI: 10.1021/acsami.5b06944
ACS Appl. Mater. Interfaces 2015, 7, 25247−25258

layer or electron transport layer. Understanding the interaction of fullerene derivatives and metals is important because fullerenes strongly prefer the metal interface due to their high surface energy,[23−25] and previous work has shown that C_{60} strongly interacts with metals, undergoing charge transfer with essentially any metallic species to form fullerene:metal salts (some of which can act as superconductors).[26−31]

In addition to the fact that metals can strongly interact with fullerenes, there are several additional reasons to expect that metal/fullerene interfaces might not be so simple. It is well-known, for example, that evaporated metals can penetrate through films of organic molecules that are a few nanometers thick, allowing the creation of "memistors" and other devices that originally were expected to behave as simple capacitors or tunnel junctions.[32] The nature of organic layer/metal contacts also has been studied in films of small molecules such as pentacene,[33,34] tris-8-hydroxyquinolinato-aluminum (Alq_3),[35,36] and diindenoperylene (DIP),[33,37] where it has been established that even though nearly all the metal remains on top of the organic layer, small amounts of evaporated metal can penetrate to the bottom of ∼60 nm thick films. A diffusion depth of ∼2 nm of Au atoms into amorphous polystyrene films during sputtering also has been reported previously.[38]

There are important reasons to investigate the penetration of commonly evaporated electrode metals into layers of fullerenes, particularly in device physics experiments. For example, the reduction of the effective active-layer thickness by metal penetration can impact measurements that require accurate knowledge of the (electrical) thickness of fullerene-based devices (e.g., space-charge limited current, time-of-flight measurements, charge extraction, etc.).[33,34,39−41] Moreover, excessive metal penetration likely causes increased leakage current[42,43] and exciton quenching,[44] produces alterations of the active-region energy band structure,[45,46] and affects device stability.[47,48] Finally, metal interpenetration is expected to play an important role in OPVs because certain fullerene derivatives preferentially segregate toward the air interface. For example, OPV active layers formed from novel polymer:fullerene blends such as PCPDTBT:ICBA[49] and PSPDTTBT:ICBA,[50] unlike the (thermally annealed) workhorse materials P3HT:PCBM,[51] are known to have fullerene-rich layers on the top of the underlying polymer/fullerene blend. Moreover, many polymer:fullerene OPVs are now formed via sequential processing, where the fullerene is deposited on top of a preformed polymer film, leading to a fullerene-rich top surface.[52−57]

In this work, we show that evaporated electrode metals penetrate extensively, through many tens of nanometers, into films of both pure fullerene derivatives and the fullerene-rich upper portion of OPV active layers. By using a combination of capacitance measurements, cross-sectional transmission electron microscopy (X-TEM), and UV−visible spectroscopy on fullerene/evaporated metal layers in various device geometries, we find that commonly used electrode metals, including Au, Al, Ag, and Ca, all readily penetrate extensively through thick fullerene-derivative layers, significantly altering both the optical and electrical properties of the devices. Our electrical measurements show that the effective electrical thickness of fullerene-based devices, as measured by their geometric capacitance, can easily change by 70 nm, a result confirmed by electron microscopy images. For the particular case of Au evaporated onto as-cast sequentially processed poly(3-hexylthiophene) (P3HT)/[6,6]-phenyl-C_{61}-butyric acid methyl ester (PCBM) quasi-bilayers,[52−54] we show that metal penetration results in the formation of ∼3−20 nm diameter nanoparticles (NPs) that are embedded throughout the PCBM overlayer matrix. This not only indicates an exceptionally high penetration/diffusivity of the metal into the fullerene[58,59] but also results in readily measurable plasmonic effects from the NPs, which can alter the optical properties of the device and which could possibly be used to advantage. Because fullerene-rich top layers paired with evaporated metals such as Au, Ca, Ag, and Al are critical components of OPV and perovskite-based solar cells as well as transistors and other organic electronic devices,[11,43,44,47,60−63] the fact that metals can extensively penetrate into fullerene derivatives has important implications for the organic electronics research community.

2. EXPERIMENTAL SECTION

2.1. Fabrication of Diodes with Fullerene and Polymer/Fulllerene Active Layers. We used P3HT (Rieke Metals, Inc. Sepiolid P100), and PCBM (Nano-C, 99.5% purity, used as received) materials for all devices. We found that the quality of the P3HT batch was important, because low molecular weight or regiorandom material tends to segregate to the top of sequentially processed PCBM overlayers during casting of the fullerene, blocking metal penetration. The use of highly regioregular P3HT that has been doubly-extracted with dichloromethane (DCM)[52] also prevents the materials from intermixing too much during PCBM casting, so that P3HT does not block the metal penetration.

All devices with polymer in the active layer were fabricated by first sequentially sonicating ITO-coated (150 nm, 20−25 Ω/□) glass substrates in acetone and isopropyl alcohol, respectively. We then dried the substrates and further cleaned them in a UV-ozone reactor for ∼20 min, which was immediately followed by the spin-coating of a ∼35 nm thick PEDOT:PSS (Clevios P VP AI 4083) layer onto the ITO-coated glass. The PEDOT-coated substrates were then thermally annealed at 150 °C for 15 min in order to drive off residual water. After PEDOT deposition and baking, we spin-coated the P3HT layer from an ODCB solution, always keeping the polymer concentration at 20 mg/mL. For sequentially processed devices, we first spun the P3HT solution at 1000 rpm for 60 s, which resulted in fully dried P3HT films that were ∼115−130 nm thick. These P3HT films were then placed in an evacuated antechamber for at least 1 h to remove any residual ODCB solvent. If placed under vacuum for an insufficient time, the ODCB remaining in the P3HT underlayer promoted intermixing of the P3HT with the PCBM overlayer, which substantially hindered metal penetration.

After the vacuum drying process, we deposited the PCBM layer from a DCM solution at 10 mg/mL concentration at 4000 rpm for 10 s. Different PCBM overlayer thicknesses were obtained by adjusting the PCBM concentration in DCM. For devices with pure PCBM as the active layer, Si-based substrates were prepared in an identical manner to the ITO substrates and the PCBM layer was spun from a 10 mg/mL PCBM solution at 1000 rpm for 20 s. Finally, we deposited metal electrodes with an Angstrom Engineering, Inc. evaporator at a pressure of $\leq 1 \times 10^{-6}$ Torr. All initial metal layers were typically deposited at a rate of 0.1−0.5 Å/s to a thickness of 10 nm, and the subsequent layer was deposited at a rate of 1.5 Å/s to thicknesses of ≥40 nm. Before the devices were exposed, ∼5−10 nm of material was typically evaporated onto the shutter to ensure layer purity. Film thicknesses were measured with a profilometer (Dektak).

For the devices with a structure of ITO/ZnO/organic semiconductor/MoO_3/Ag, the ZnO nanoparticle solution was synthesized following the method by Beek et al.[64] and then spun onto cleaned ITO substrates from chloroform to form a 40 nm ZnO layer, as confirmed by profilometry. These ZnO-coated substrates were then annealed at 150 °C in a nitrogen glovebox for 20 min. After the organic layer fabrication, a 15 nm MoO_3 layer was deposited on top of the organic layer at rates below 0.5 Å/s, followed by a 70 nm Ag layer deposited at rates below 1.0 Å/s.

DOI: 10.1021/acsami.5b06944
ACS Appl. Mater. Interfaces 2015, 7, 25247−25258

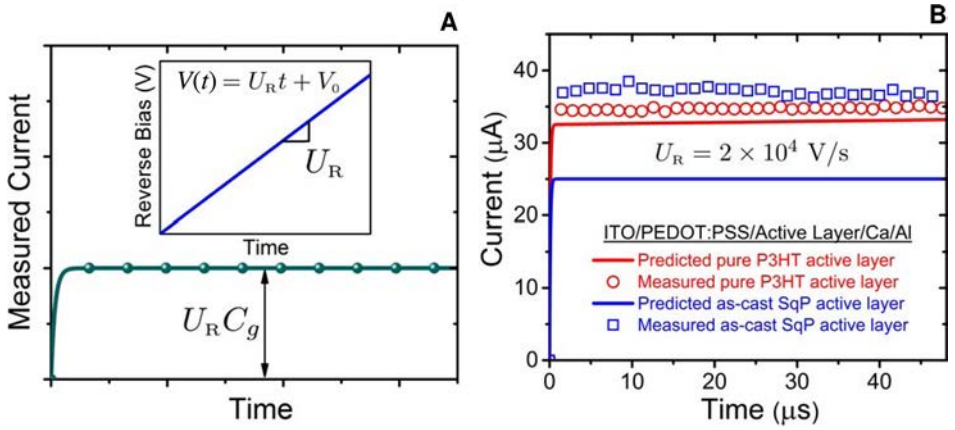

Figure 1. (A) Schematic of how C_g is measured straightforwardly in the CELIV experiment. More details on the mathematical extraction of C_g from CELIV traces are given in the Supporting Information. (B) Measured reverse-bias CELIV current transients of ITO/PEDOT:PSS/P3HT(115 nm)/PCBM(66 nm)/Ca/Al devices showing a distinct difference between the predicted (solid curves, from eq 1 using the measured layer thickness(es) and dielectric constant(s)) and measured C_g values (open symbols) when a PCBM-rich overlayer (sequentially processed quasi-bilayer) is added on top of the P3HT and then exposed to the evaporated metal electrode. Note that $V_0 = 0$ for the pure P3HT capacitor (no equilibrium free charge), but a V_0 value of −3 V was needed for the quasi-bilayer in order to ensure that the active layer was fully depleted.

2.2. CELIV Experiment for Determination of C_g. For a description of the analytical CELIV analysis approach, see the Supporting Information and ref 53. Experimentally, we measured CELIV traces with a DS345 function generator paired with a Tektronix DPO 3014 150 MHz digital oscilloscope.[53]

2.3. FIB Processing, Cross-Sectional TEM, and Sample Preparation. The as-cast P3HT/PCBM quasi-bilayer device made by sequential processing was imaged in a FEI Titan S/TEM instrument operated at 300 kV. As described in the Supporting Information, we were careful to limit any potential electron beam damage.[65,66] Our cross-sectional TEM samples were prepared using typical lift-out methods in an FEI Nova 600 Nanolab DualBeam Ga FIB system. Prior to milling, the surface was protected with a ∼2 μm thick layer of Pt deposited first by electron beam, then by ion beam. Side-by-side trenches were cut into the bulk substrate to create a ∼20 μm × 2 μm thin section, which was then partially milled from the substrate by a U-cut. Next, the detached end of the sample was attached to a nanomanipulator needle, the opposite end was milled completely out of the substrate, and the sample was adhered with ion-beam-deposited Pt to a commercial Cu lift-out grid. The needle tip and excess Pt were cut out, and the sample was further thinned to electron transparency. The final thinning process was executed at the low-power conditions of 10 kV beam energy, 40 nm beam diameter, and 0.12 nA probe current.[67] The final step involved making a 2° wedge-shaped sample with thinner top and thicker bottom for structural integrity.

2.4. XPS for Determination of Surface Composition. Surface volume percent calculation details can be found in the Supporting Information,[68] whereas the experimental apparatus and approach are described in detail in ref 53.

2.5. Spectroscopic Ellipsometry for Layer Thickness. The organic layer thicknesses that were determined by spectroscopic ellipsometry were obtained by fitting the transparent region of the material to a thickness/Cauchy-dispersion model. All of these values were obtained from equivalently processed layers deposited on a Si/(1.8 nm SiO_2 native oxide) substrate. The thick SiO_2 thermal oxide values reported in the text were determined by fitting the entire $\tan(\Psi)$, $\cos(\Delta)$ spectrum to the well-known optical constants of SiO_2 and Si (SOPRA *nk* library). A detailed description of the experimental setup and procedures can be found elsewhere.[55]

3. RESULTS AND DISCUSSION

3.1. Electrical Thickness of Fullerene Films Measured via Device Geometric Capacitance. Our initial evidence for the interpenetration of evaporated metals into fullerene-rich layers comes from simple electrical characterization experiments. We started by measuring the geometric capacitance (C_g) of standard planar fullerene-based devices with different active layers using the charge extraction by linearly increasing voltage (CELIV) technique.[69,70] The CELIV approach for obtaining C_g is schematically shown in Figure 1A, and involves using (if necessary) an initial steady-state reverse bias to deplete fully the active layer of any equilibrium free charge. The experiment is also run in the dark, which eliminates the presence of photogenerated carriers. The initial bias is followed by a linear reverse-bias ramp of the form $V(t) = U_R t + V_0$ where t is the time after the start of the ramp, V_0 is the initial steady-state reverse bias, and U_R is the ramp rate (V/s). For a typical parallel-plate capacitor, the current response to this voltage ramp is constant in time and directly related to C_g (Figure 1A). Because the device is initially depleted and the voltage ramp is run in reverse bias, the device behaves essentially as a capacitor. It is thus straightforward to fit the CELIV current transients to an equivalent circuit model, described in the Supporting Information, in order to extract accurately C_g.

One of the reasons CELIV is particularly well-suited for measuring C_g is because it allows for easy decoupling of the geometric capacitance from other quantities, such as the equilibrium doping density, series/shunt resistances, and the device's built-in potential.[40,71,72] The geometric capacitance is determined solely by the device's geometry, with $C_g = A\epsilon_0\epsilon/d$ for a simple single-layer capacitor, where A is the device area, ϵ_0 is the vacuum permittivity, ϵ is the dielectric constant of the material between the electrodes, and d is the electrical thickness of the device. Thus, we have chosen to focus on the device C_g because it provides an excellent indicator of metal penetration due to its high sensitivity to the active-layer dielectric constant and electrical thickness, both of which are strongly impacted by the incorporation of metal.

Our discovery of metal interpenetration took place when we were examining CELIV transients on OPV devices based on P3HT and PCBM. We built numerous devices via solution sequential processing (SqP) of the active layer,[55,73] where the polymer layer is deposited first, in this case from *o*-dichlorobenzene (ODCB), and then the fullerene layer is deposited in a second step from a quasi-orthogonal solvent, in

DOI: 10.1021/acsami.5b06944
ACS Appl. Mater. Interfaces 2015, 7, 25247−25258

Table 1. Measured and Predicted Geometric Capacitance (C_g) Based on the Measured Active-Layer Thickness for Various Organic Semiconductor Diodes[a]

active layer	evaporated electrode[a]	measured C_g (nF)	calculated C_g (nF)	measured thickness[b] (nm)	C_g thickness[c] (nm)
P3HT[d]	Ca/Al	1.74 ± 0.09	1.68 ± 0.08	115 ± 5	110 ± 6
P3HT	MoO_3	1.39 ± 0.01	1.39 ± 0.01	115 ± 5	115 ± 1
PCBM (80 nm)	Ca/Al	shorted	3.11 ± 0.19	80 ± 5	
PCBM (80 nm)	MoO_3	2.27 ± 0.01	2.30 ± 0.19	80 ± 5	79 ± 1
P3HT/PCBM (37 nm) SqP	Ca/Al	1.83 ± 0.12	1.41 ± 0.12	152 ± 5	111 ± 7
P3HT/PCBM (66 nm) SqP	Ca/Al	1.81 ± 0.13	1.21 ± 0.10	181 ± 5	115 ± 8
P3HT/PCBM (75 nm) SqP	Ca/Al	1.78 ± 0.03	1.16 ± 0.09	190 ± 5	118 ± 2
P3HT/PCBM, 150 °C SqP	Ca/Al	1.29 ± 0.02	1.25 ± 0.09	178 ± 5	171 ± 3
P3HT/PCBM, 110 °C SqP	Ca/Al	1.51 ± 0.09	1.29 ± 0.10	178 ± 5	147 ± 9
P3HT:PCBM, 150 °C Blend-Cast	Ca/Al	1.25 ± 0.07	1.30 ± 0.04	173 ± 5	177 ± 10
P3HT/PCBM SqP	Ca (0.3 nm)/Ag	1.87 ± 0.16	1.21 ± 0.10	181 ± 5	112 ± 10
P3HT/PCBM SqP	Al	1.78 ± 0.19	1.21 ± 0.10	181 ± 5	117 ± 12
P3HT/PCBM SqP	Mg	2.40 ± 0.02	1.21 ± 0.10	181 ± 5	87 ± 9
P3HT/PCBM SqP	Au	2.01 ± 0.06	1.21 ± 0.10	181 ± 5	104 ± 3
P3HT/PCBM SqP	Ag	shorted	1.21 ± 0.10	181 ± 5	
P3HT/PCBM SqP	Pt[e]	shorted	1.21 ± 0.10	181 ± 5	
P3HT/PCBM SqP	Na (15 nm)/Ag	shorted	1.21 ± 0.10	181 ± 5	
P3HT/PCBM SqP	K (15 nm)/Ag	shorted	1.21 ± 0.10	181 ± 5	
P3HT/bis-PCBM SqP	Ca/Al	2.16 ± 0.20	1.21 ± 0.10	176 ± 5	97 ± 9
P3HT/ICBA[f] SqP	Ag	shorted	<1.21	>181	
P3HT/ICBA SqP	Ca (45 nm)	2.52	<1.21	>181	89
P3HT/ICBA SqP	Al	3.11	<1.21	>181	72
SiO_2 (270 nm)	Ca/Al	1.55 ± 0.01	1.55 ± 0.1	270[f]	270 ± 2
SiO_2 (285 nm)/PCBM (95 nm)	Ca/Al	1.35 ± 0.03	1.10 ± 0.1	380[g]	310 ± 3

[a]If not specified, the thickness for Ca is 10 nm, for Al is 70 nm, for Ag is 70 nm, for MoO_3 is 15 nm, and for ZnO is 40 nm. The corresponding underlayer for MoO_3 was ZnO and the corresponding underlayer for all metals was 35 nm of PEDOT:PSS (Clevios P VP Al 4083) unless otherwise noted. [b]All thickness values are determined by profilometry and refer to the organic layer(s) only, except for the last two rows. [c]Calculated from measured C_g. [d]P3HT C_g is sensitive to polymer batch and thermal annealing. [e]The e-beam deposited to 50 nm at less than 0.5 Å/s rate. [f]The ICBA-based SqP devices were thicker than their PCBM counterparts but with indeterminate thickness due to surface roughness. [g]SiO_2 contribution determined by spectroscopic ellipsometry and PCBM contribution determined by both profilometry and spectroscopic ellipsometry.

this case DCM. We used the active layers as-cast without thermal or solvent annealing, which results in devices with a quasi-bilayer geometry: ITO/PEDOT:PSS/P3HT/PCBM/metal.[56,57,74] Because the top of the active layer of these devices is rich in PCBM,[53,56,57,74] this provided a perfect opportunity to observe how evaporated metal electrodes interacted with fullerene-rich layers in sandwich-structure devices. Our experiments explored as-cast sequentially processed devices with varying active layer compositions, thicknesses, and evaporated electrodes (see Table 1). In all cases, we directly measured the thickness of the active layer using profilometry, which has an accuracy of ±5 nm. Figure 1B shows an example of the results, where the red circles are for a device with a pure 115 nm thick P3HT film as the active layer, and the blue squares are for a device with an active layer consisting of an identically processed P3HT film with a ∼66 nm thick solution sequentially processed PCBM overlayer. Surprisingly, even though the 181 nm thick sequentially processed active layer is significantly thicker than the pure P3HT layer, the sequentially processed device actually has a slightly higher capacitive current and thus a slightly larger geometric capacitance.

To analyze the geometric capacitances of our devices obtained from CELIV, we calculated the C_g values for pure active layers from the parallel-plate capacitor relation: $C_g = A\epsilon_0\epsilon/d$, with typical values for P3HT layers of $d_{P3HT} = 115 \pm 5$ nm, $A = 7.2 \pm 0.5$ mm^2 (we used this electrode area for all devices unless otherwise specified), and $\epsilon_{P3HT} = 3 \pm 0.1$.[75] For the sequentially processed devices with fullerene overlayers, we assumed a bilayer parallel-plate geometry, where fullerene penetrates into the polymer film producing a mixed underlayer,[74] plus an essentially pure fullerene layer on top, resulting in

$$C_g = \frac{A\epsilon_0\epsilon_{P3HT:PCBM}\epsilon_{PCBM}}{d_{PCBM}\epsilon_{P3HT:PCBM} + d_{P3HT:PCBM}\epsilon_{PCBM}} \quad (1)$$

where for the devices in Figure 1B, $\epsilon_{PCBM} = 3.9 \pm 0.1$,[75] and $d_{PCBM} = 66 \pm 5$ nm. Previous work using neutron reflectometry on as-cast sequentially processed P3HT/PCBM active layers found that the P3HT-rich underlayer contains ∼25−30 wt % PCBM and that the underlayer does not change appreciably in thickness.[56,57,74] Using this information and the effective medium approximation, we employed typical values of $d_{P3HT:PCBM} = 115 \pm 5$ nm and $\epsilon_{P3HT:PCBM} = 3.25 \pm 0.1$ for the P3HT-rich underlayer. The uncertainties quoted here lead directly to those quoted for C_g in Table 1 using standard propagation of errors.[76]

A further statistical comparison of numerous devices processed identically to those shown in Figure 1B reveals that pure P3HT devices of this thickness should have a C_g value of 1.66 ± 0.08 nF, which is in good agreement with the measured value of 1.74 ± 0.09 nF. In contrast, the sequentially processed quasi-bilayer has a predicted C_g value of 1.25 ± 0.1 nF, which is well outside the error of the measured value. The fact that the measured C_g value for the quasi-bilayer is significantly larger than expected indicates that the effective

DOI: 10.1021/acsami.5b06944
ACS Appl. Mater. Interfaces 2015, 7, 25247−25258

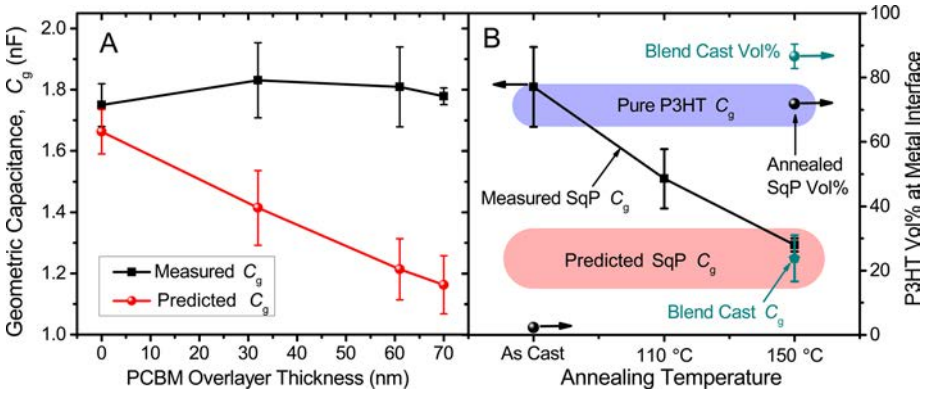

Figure 2. (A) Measured and predicted geometric capacitances of P3HT/PCBM/Ca/Al sequentially processed as-cast quasi-bilayer devices with different PCBM overlayer thicknesses. The divergence of the measured and predicted C_g values indicates metal interpenetration through the entire fullerene overlayer. (B) Device geometric capacitance as a function of quasi-bilayer active-layer annealing temperature before metal deposition (black line; error bars one standard deviation). All devices were thermally annealed for 20 min prior to metal deposition. The evaporation rate for Ca was ~0.5 Å/s and for Al was ~1.0 Å/s. The thick blue bar represents the measured pure P3HT underlayer geometric capacitance with ± one standard deviation uncertainty. The thick pink bar represents the predicted device C_g with uncertainty calculated using the measured active-layer thickness. Annealing as-cast quasi-bilayers intermixes the P3HT and PCBM, which causes the measured C_g to approach the predicted C_g due to blocking of the metal-penetration by the presence of P3HT at the top interface. The right vertical axis shows P3HT volume percent at the top surface (black spheres; obtained from XPS S/C analysis[68]). Traditional blend-cast devices (dark cyan symbols) also show no measurable metal penetration due to the presence of nearly pure P3HT at the top surface of the active layer (dark cyan sphere).

electrical thickness of the device is much thinner than anticipated, and in fact, this device has essentially the same electrical thickness as the original P3HT underlayer (Table 1).

The only simple explanation for this discrepancy between the measured and predicted C_g values is that in the quasi-bilayer samples, the evaporated Ca/Al electrode penetrates entirely through the PCBM-rich overlayer and only stops at the P3HT-rich interface, so that the quasi-bilayer C_g values become identical to those of the pure underlayer. Despite the fact that the C_g values indicate that metal is penetrating a significant distance into the organic layer, none of these devices in Figure 1 were shorted or leaky, as evidenced by the roughly constant current versus time, confirming that the metal does not penetrate the entire organic layer. Table 1 presents measured and predicted C_g values for a number of as-cast P3HT/PCBM SqP quasi-bilayer devices with different evaporated metal electrodes (Ca/Al, Ca, Al, Mg, Ag, Pt, K, Na, and Au) and varying PCBM overlayer thicknesses, all of which exhibit discrepancies between the measured and predicted geometric capacitances that are consistent with significant metal penetration into the active layers. In particular, the C_g values in Table 1 indicate that Au, Al, and Ca electrodes penetrate entirely through the fullerene-rich overlayer but not into the P3HT-rich underlayer, and that Ag, Mg, Pt, K, and Na can actually penetrate through the fullerene-rich overlayer and into the P3HT-rich underlayer as well (Table 1). We note that the diffusion of alkali metals in polymers has been studied by others,[77] who argued that alkali metals ionize in contact with most polymers and thus are highly mobile both because positive ions repel each other, preventing agglomeration of the metal, and because cations are smaller than neutral metal atoms. These ideas are consistent with the results of our C_g analysis.

To evaluate how far the evaporated metal can penetrate through a fullerene-rich overlayer, we next analyzed the geometric capacitances of P3HT/PCBM quasi-bilayers as the thickness of the PCBM overlayer was varied. Figure 2A shows a strong divergence between the measured and predicted C_g values for P3HT/PCBM/Ca/Al devices when the PCBM overlayer is made successively thicker by increasing the PCBM concentration of the casting solution (at 4000 rpm, a 5 mg/mL solution of PCBM in DCM gives a 37 nm PCBM overlayer, a 10 mg/mL solution results in a 66 nm thick overlayer, and a 15 mg/mL near-saturated solution yields a 75 nm thick overlayer). For all these devices, it is particularly striking that the measured C_g remains constant and approximately equal to that of the pure P3HT underlayer despite the additional PCBM overlayer thickness. This is a strong indication that metal penetration can occur through PCBM overlayers of essentially any thickness obtainable by spin-coating. This result also indicates that any metal−organic "salts" formed by the reaction of the metals with the polymer likely reside only near the interface and do not penetrate through the entire fullerene layer (because otherwise the measured C_g values for SqP devices with different thicknesses would not be similar). Thus, the slight increase in capacitance observed with fullerene incorporation in Figures 2A and 1B (blue squares vs red circles) could reflect the formation of a high-dielectric salt near the surface, but more likely results either from a small amount of the P3HT underlayer being washed away by the DCM fullerene-casting solvent or from an increase in the dielectric constant of the underlayer, as PCBM has a higher dielectric constant than P3HT and the SqP approach results in ~25−30 wt % intercalation of PCBM into the P3HT underlayer.[74]

In addition to diodes built with pure P3HT active layers and P3HT/PCBM quasi-bilayers (as in Figure 1B), we also fabricated devices with well-mixed P3HT:PCBM active layers using both traditional blend-casting and thermal annealing of the sequentially processed quasi-bilayers. It is well-known that annealing P3HT/PCBM quasi-bilayers results in rapid interdiffusion of the two components,[56,57,74,78] transforming the quasi-bilayer into a more well-mixed P3HT:PCBM bulk heterojunction film. Because the degree of mixing increases as the temperature is raised above 110 °C,[57] we expect annealing at temperatures above this threshold to increase significantly the amount of P3HT that resides at the top surface of the active layer. In all our experiments, metal evaporation was performed after thermal annealing of the quasi-bilayer. This leads to an

DOI: 10.1021/acsami.5b06944
ACS Appl. Mater. Interfaces 2015, 7, 25247−25258

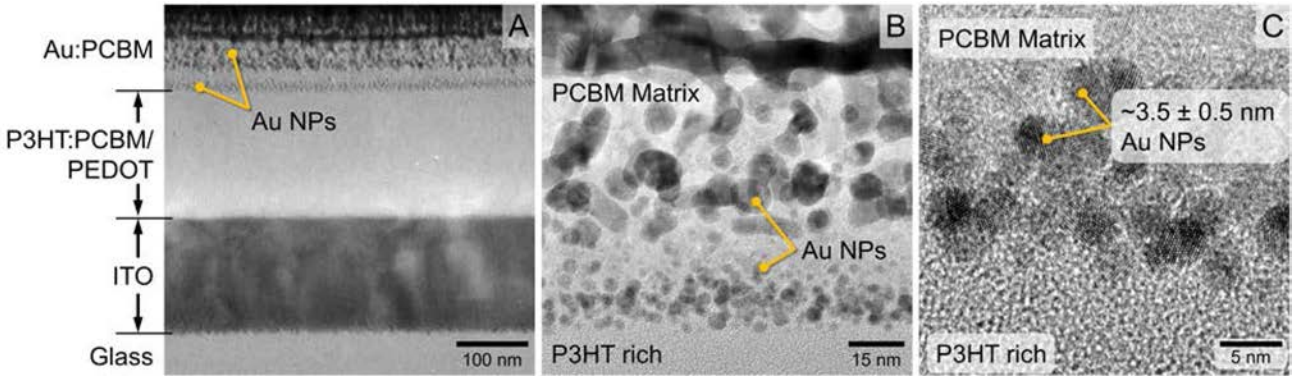

Figure 3. Bright-field, cross-sectional TEM images of a glass/ITO/PEDOT:PSS/P3HT:PCBM/PCBM:Au/Au as-cast, sequentially processed quasi-bilayer device (the same device used in the C_g analysis in the previous section). (A) Representative section of the entire device stack and each layer's persistence in the in-plane direction. (B) Higher magnification view of the P3HT:PCBM/PCBM:Au/Au interfaces, showing the clear formation of metal nanoparticles resulting from the thermal evaporation of Au onto the PCBM-rich portion of the active layer. (C) Further magnified view of the region just above the interface with the P3HT-rich underlayer, showing a layer of fairly monodisperse ~3.5 ± 0.5 nm diameter Au nanocrystals. Gold was chosen as the electrode metal for these experiments due to its high *Z*-contrast with the organic layer and its stability in air. The evaporation rate for the gold electrode was kept <0.5 Å/s.

expectation that the more annealed the film, the more P3HT will cover the top surface, so less metal penetration should result. Indeed, Figure 2B shows that the measured C_g of annealed P3HT/PCBM quasi-bilayers steadily decreases with increasing annealing temperature from 110 to 150 °C. Moreover, when the mixing becomes strong enough (by annealing for 20 min at 150 °C) the measured C_g becomes, within error, equal to the predicted C_g based on the measured active-layer thickness. Also plotted in Figure 2B is the C_g of a blend-cast P3HT:PCBM device that has the same total thickness and composition as the quasi-bilayer devices.[53] The C_g of this blend-cast device also shows no deviation between the measured and predicted C_g values, consistent with the idea that blend-casting produces devices with large amounts of P3HT on the top surface.

All of these results suggest that even small amounts of P3HT at the top surface of the active layer can block metal penetration in the same way that a P3HT-rich underlayer stops metal interpenetration from completely shorting a quasi-bilayer device. To quantify better this effect, we measured the surface composition of these active layers using X-ray photoelectron spectroscopy (XPS). For the P3HT/PCBM system, the measured XPS sulfur/carbon ratio provides a direct measure of the amount of P3HT in the top few nanometers of the active layer.[53,68] The right vertical axis of Figure 2B shows the volume percent of P3HT at the top surface of each of these samples as determined by XPS (see the Supporting Information for S/C calculation details). The data show that 150 °C-annealed quasi-bilayers and traditional blend-cast P3HT:PCBM active layers have >70 vol % P3HT at their top surfaces, whereas as-cast P3HT/PCBM quasi-bilayers only have ~3 vol % P3HT at their surfaces. Clearly, Figure 2B suggests that evaporated metal electrodes can easily penetrate through fullerene-rich layers but cannot penetrate through even a small amount of dilute conjugated polymer such as P3HT. Taken together, the C_g analysis in Figures 1 and 2 and Table 1 leads to three major conclusions: first, that the device geometric capacitance is a reliable indicator of metal penetration; second, that the functional device structure is dramatically changed when an electrode metal is evaporated onto a PCBM-rich layer; and third, that P3HT acts as a remarkably efficient blocker of metal penetration.

Because the presence of even small amounts of P3HT at the top surface can affect metal penetration, it makes sense to investigate the interaction of evaporated metals with pure fullerene films. Table 1 shows that when we fabricated diodes with a pure PCBM active layer (device structure ITO/PEDOT:PSS/PCBM/Ca/Al), the devices were always either shorted or too leaky to obtain reliable C_g values. This indicates that the evaporated electrode can effectively penetrate through the entire fullerene layer to make electrical contact with the bottom electrode, consistent with the quasi-bilayer results discussed above. To verify that there is nothing special about P3HT stopping metal interpenetration, Table 1 also summarizes results indicating metal penetration can be blocked by placing a thin insulating interlayer (e.g., 15 nm of MoO_3, which is typically used to fabricate "inverted" OPV devices[24,79]) on top of the fullerene layer; see also Figure S5 of the Supporting Information. This observation might be an important reason why inverted device architectures that utilize metal oxide buffer layers typically work better than their normal-structure counterparts for OPVs,[79−81] as metal interpenetration could easily be detrimental to solar cell performance. Finally, Table 1 also shows that we obtained identical C_g trends using other fullerene derivatives, including indene-C_{60} bisadduct (ICBA)[82] and bis-PCBM,[83] demonstrating that evaporated metal interpenetration is a general phenomenon for many fullerene derivatives.

As another way to investigate evaporated metal penetration into pure fullerene films, we also fabricated devices using doped Si with a thick thermal oxide overlayer as the bottom electrode. Table 1 shows that when a Ca/Al top electrode is evaporated directly onto the thick SiO_2 thermal oxide layer, the measured C_g of the resulting device is in excellent agreement with the parallel-plate capacitor equation prediction: $C_g = A\epsilon_0\epsilon_{SiO_2}/d_{SiO_2}$ = 1.55 nF, with d_{SiO_2} = 270 nm, ϵ_{SiO_2} = 3.9, and A = 12.1 mm^2. However, when 95 nm of PCBM (as measured by profilometry and spectroscopic ellipsometry) is spun on top of the SiO_2 overlayer, the measured C_g is just 1.35 nF (with the same Ca/Al top electrode), which is much larger than that predicted and only slightly smaller than that of the device built without PCBM. A simple analysis reveals that this C_g value accounts for only ~25 nm of the PCBM layer, leaving ~70 nm of PCBM

DOI: 10.1021/acsami.5b06944
ACS Appl. Mater. Interfaces 2015, 7, 25247−25258

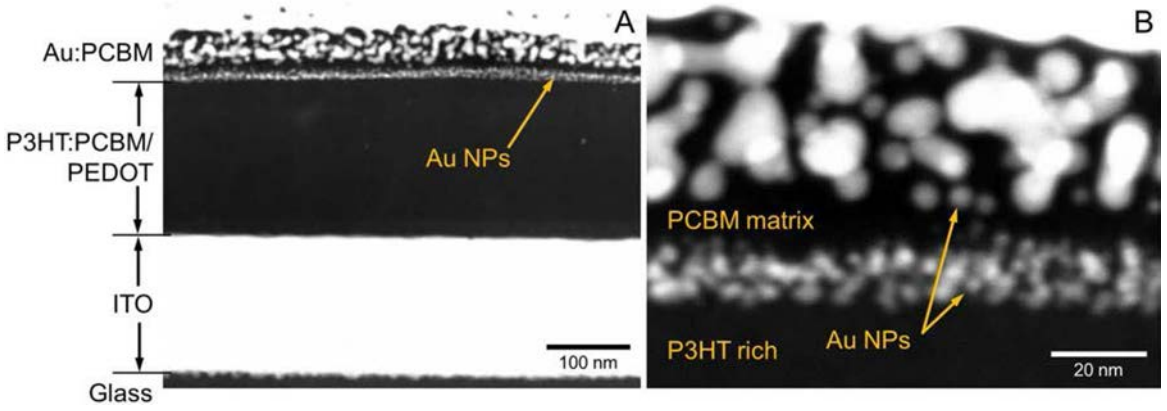

Figure 4. HAADF STEM images of the same device cross section studied in Figure 3. (A) Lower magnification view, showing each distinct layer of the device as labeled. (B) Higher magnification view of the P3HT:PCBM/PCBM:Au/Au interface. The high contrast between the Au nanoparticles and the surrounding PCBM matrix indicates extensive phase separation of the metal and the organic materials.

'missing' from the dielectric thickness. This demonstrates that the evaporated Au electrode has an effective electronic penetration depth of approximately 70 nm into the 95 nm thick PCBM film. These data indicate that either the top 70 nm of the fullerene layer has become a part of the electrode or that the dielectric constant of this portion of the film has become so high because of the amount of intercalated metal that it essentially has no measurable capacitance when placed in series with the effective ∼25 nm of "pure" PCBM.

3.2. X-TEM Analysis of Metal Interpenetration in PCBM Films. With ample evidence in hand for metal penetration, the obvious question becomes: can we directly observe and measure the infiltrated metal distribution inside these fullerene layers? To address this question, we turn to cross-sectional transmission electron microscopy (X-TEM), where a focused-ion beam (FIB) is used to cut a thin section from an as-cast, sequentially processed P3HT/PCBM quasi-bilayer device, and the resulting device cross section is directly imaged with TEM.[21,52,84,85] To generate a sample for this process, we evaporated a Au top electrode onto an as-cast P3HT/PCBM quasi-bilayer active layer at a rate of only 0.1 Å/s, leading to an expected device architecture of glass/ITO (150 nm)/PEDOT:PSS (35 nm)/P3HT:PCBM (130 nm)/PCBM (45 nm)/Au (50 nm); here, as above, we expect the P3HT:PCBM underlayer to have ∼25−30 wt % PCBM from the SqP.[74] When collecting this data, care was taken to limit electron beam exposure and any subsequent possible sample damage.[65,66,86] We note, however, that our primary interest in this work is the structure of the interpenetrated metal, which is robust to beam exposure. We chose to use gold as the evaporated top electrode material for three reasons: first, the capacitance measurements described above indicate that Au can penetrate up to ∼70 nm into fullerene-rich films; second, Au has excellent *Z*-contrast in comparison to the carbon-based P3HT/PCBM active-layer materials; and third, Au does not readily degrade or oxidize, making it robust to the necessary processing steps leading up to TEM imaging.

Figure 3A clearly shows that instead of the nominally fabricated glass/ITO/PEDOT:PSS/P3HT:PCBM/PCBM/Au device structure, there is indeed readily visible Au metal penetration into the PCBM overlayer. Further inspection suggests that a more accurate description of the actual device architecture is glass/ITO/PEDOT:PSS/P3HT:PCBM/PCBM:Au/Au, with clear distinct boundaries for each of these layers. We used high-angle annular dark-field (HAADF) scanning transmission electron microscopy (STEM), discussed below, and spot EDS spectra, shown in the Supporting Information, to verify the elemental composition in each region of the image. One of the most striking and unexpected features of Figure 3A is a distinct layer of Au nanoparticles (NPs) that is visible ∼175 nm above the ITO/PEDOT:PSS interface. This distance is consistent with the nominal thickness of the P3HT-rich underlayer plus PEDOT:PSS interlayer, indicating that Au penetration proceeds all the way down to the P3HT-rich layer. This may seem surprising given that P3HT has a lower mass density than PCBM,[87] but is in perfect agreement with the conclusions reached above from our C_g analysis. We hypothesize that the sulfur heteroatom in the polymer plays a role in stopping metal penetration, because gold, for example, has an otherwise high diffusivity in conjugated carbonaceous systems.[58,59] In the P3HT/Ca system, for instance, it has been shown that the Ca/S-heteroatom interaction is significant enough to abstract the sulfur from P3HT.[88,89]

Figure 3B focuses on what should have been the P3HT/PCBM quasi-bilayer interface,[56,57,74] but instead is found to be a PCBM:Au-NP matrix in contact with the P3HT-rich underlayer. This image reveals that moving upward from the P3HT-rich underlayer interface, there is first a dense region of small (∼3.5 nm diameter) Au NPs located at and just above the interface, followed by a PCBM-rich region that contains very little Au, followed by a PCBM-rich layer that contains larger-sized (∼10−20 nm diameter) Au particles. Figure 3C shows higher magnification of the small Au NP layer just above the P3HT-rich interface, making clear that the spontaneously formed Au NPs are highly crystalline (see also the selected-area electron diffraction pattern in Figure S4 of the Supporting Information). These particles are nominally spherical and fairly monodisperse in size with diameters in the range of 3.5 ± 0.5 nm. Not only is this type of NP formation at the bottom of a thick organic layer extremely rare, but the pattern of small Au nanoparticles, pure organic layer, then larger Au NPs is completely different than that observed in previous interpenetration studies.[37] We postulate that the P3HT-rich underlayer has much to do with both the metal NP formation and distribution. There likely is a small amount of P3HT in the PCBM-rich overlayer (because SqP does mix the polymer and fullerene components, as indicated by the XPS data of Figure

DOI: 10.1021/acsami.5b06944
ACS Appl. Mater. Interfaces 2015, 7, 25247−25258

2).[56,57] Given that P3HT interacts strongly with the penetrated metal, it is entirely possible that the few P3HT chains dissolved in the PCBM-rich overlayer act as nucleation sites for the penetrated Au to grow into NPs, leading to the observed nanostructure.

3.3. HAADF X-TEM Analysis. To visualize better the compositional nanostructure studied in Figure 3, we employed STEM HAADF imaging of this same device cross section. HAADF STEM is not influenced by diffraction effects and primarily reveals variations in atomic mass density (*Z*-contrast), making it ideal for examining the distribution of metallic Au in organic matrices. As expected, the HAADF images in Figure 4 show sharp contrast between the carbon-rich and gold-rich regions of the Au:PCBM layer. Figure 4A shows the entire glass/ITO/PEDOT/P3HT:PCBM/PCBM:Au/Au layer stack, confirming that the layered structure of each region persists throughout the in-plane direction. Notably, there are several Au NPs visible as small gray dots in the P3HT-rich layer, although it is not clear whether these particles diffused into the layer via interpenetration from above or were simply displaced during the FIB processing and are located on top of the cross-section. Figure 4A also better reveals the nonuniform Au:PCBM nanostructure seen in Figure 3A, which consists of a dense region of small, ~3.5 nm diameter gold NPs at the P3HT-rich interface, followed by a region devoid of Au, and then a thicker Au:PCBM matrix composed of large, semi-interconnected Au NPs (~10−20 nm diameter). In Figure 4B, higher magnification HAADF imaging shows high contrast (i.e., a complete lack of gray scale) between the particles and surrounding matrix, indicating essentially complete phase separation of Au in the PCBM-rich layer. The formation of discrete Au nanoparticles suggests that a significant contributor to the reduction of C_g, as discussed above, is the large increase in effective dielectric constant of the mixed metal:fullerene layer, which causes this layer to have no effective contribution to the overall device capacitance (eq 1 with $\epsilon_{PCBM:Au} \rightarrow \infty$).

Overall, Figures 3 and 4 completely change our perception of what can happen when evaporated electrode metals are deposited onto layers rich in fullerene derivatives. The fact that electrode metals penetrate many tens of nanometers into fullerene-rich layers is not only unexpected but also will clearly have a significant impact on device optoelectronic properties. Although most of the effects are deleterious, it might be possible to use the penetration to advantage, particularly if the size of the intercalated NPs can be tuned, as we discuss in the next section.

3.4. Plasmonic Effects of Interpenetrated Nanoparticles. One particularly important impact comes from the fact that interpenetrated metal need not be uniformly present in the fullerene layer, but instead can be phase-separated into NPs that are of exactly the size required for significant plasmonic effects (Figures 3 and 4).[90−93] We show that plasmonic effects can be readily measured in metal-interpenetrated fullerene films in Figure 5. In this figure, we plot the normal-incidence absorbance of a glass/PCBM (55 nm) sample both before (black curve, squares) and after (red curve, circles) the evaporation of 3 nm of gold. The blue curve in the inset shows absorption difference expected if the 3 nm Au overlayer were planar, as calculated via a transfer-matrix approach using published optical constants.[94,95] Instead, the actual change in optical density upon Au evaporation is shown by the orange curve in the inset, which has a distinct peak at ~620 nm. This peak is in the range one would expect for the collective

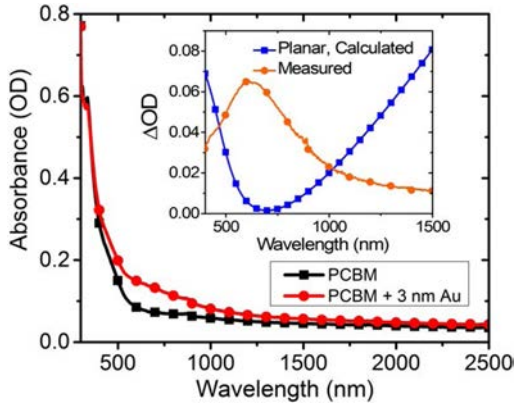

Figure 5. Normal-incidence optical density of a 55 nm PCBM layer on glass before (black curve, squares) and after (red curve, circles) thermal evaporation of 3 nm of Au. The red circles/curve in the inset shows the measured change in OD upon metal evaporation, whereas the blue squares/curve shows the expected ΔOD (calculated using a transfer matrix approach with published optical constants)[94,95] if the Au formed a 3 nm overlayer on top of the PCBM film. The fact that the observed ΔOD peaks near 600 nm is consistent with the plasmon resonance of Au NPs that have formed within the fullerene layer.

plasmon resonance of inhomogeneously distributed, interacting, Au nanoparticles.[96,97] Because the NPs formed in fullerene films are obviously bare (i.e., they have no capping agents), there should be significant near-field coupling to the organic material around the NPs. This means that the presence of metal NPs must be accounted for when performing optical modeling of any devices with evaporated metal electrodes on fullerene-rich layers. Moreover, it is possible that with appropriate design this effect could be utilized to enhance, for example, the absorption of fullerenes such as $PC_{71}BM$ that are placed intentionally at the top surface of OPVs.[90,98]

4. CONCLUSIONS

In summary, we have shown that evaporated metal electrodes significantly penetrate into films of fullerene derivatives, having substantial implications for optoelectronic devices that involve metal/fullerene interfaces (e.g., OPVs, perovskite solar cells, thin-film transistor contacts, etc.). The most direct consequence is that the effective electrical thickness of fullerene-based devices, as measured by their geometric capacitance, is dramatically reduced due to the metal incorporation. For example, we showed using a model doped-Si/SiO_2/PCBM/Au device structure that there is ~70 nm of effective Au penetration into a pure PCBM film. We also confirmed via C_g analysis that evaporated metal penetration into fullerene-rich films occurs with numerous fullerene derivatives and evaporated metal combinations, and thus is a general phenomenon that is not specific to materials such as Au and PCBM. Our X-TEM analysis shows that a striking and unexpected interpenetrated nanostructure is formed when an electrode metal is evaporated onto a fullerene-rich layer that is cast on top of a polymer-rich underlayer. Instead of yielding a clean fullerene/metal interface, metal evaporation results in extensive penetration and metal nanoparticle formation throughout the fullerene-rich layer. Furthermore, the images and C_g analysis indicate that metal penetration is efficiently stopped by the presence of even small amounts of conjugated polymers such as P3HT or insulating materials such as MoO_3. In addition to all the implications for optoelectronic device

DOI: 10.1021/acsami.5b06944
ACS Appl. Mater. Interfaces 2015, 7, 25247−25258

physics experiments, this discovery opens up a number of possibilities in terms of interface and optical engineering with fullerene semiconductor materials.

■ ASSOCIATED CONTENT

Supporting Information

The Supporting Information is available free of charge on the ACS Publications website at DOI: 10.1021/acsami.5b06944.

Details of the circuit modeling for determination of C_g, XPS analysis for determination of surface composition, EDS analysis of Au HAADF, selected-area electron diffraction (SAED) on bright-field TEM images and CELIV result on pure PCBM devices with different electrodes (PDF).

■ AUTHOR INFORMATION

Corresponding Author

*B. J. Schwartz. E-mail: schwartz@chem.ucla.edu.

Author Contributions

G.Z. and S.A.H contributed equally to this work.

Notes

The authors declare no competing financial interest.

■ ACKNOWLEDGMENTS

The authors thank Dr. Jia Ming Chen for ample administrative assistance, Dr. Liane Slaughter for insightful discussions, Noah Bodzin for making the X-TEM samples via FIB, and Amy Ferreira for preparation of the Pt-based samples. This research was supported by the National Science Foundation under grant numbers CHE-1510353 and CHE-1112569. The XPS instrument used in this work was obtained with support from the NSF, Award 0840531. J.C.A. and S.A.H. acknowledge previous support from the NSF IGERT: Materials Creation Training Program (MCTP), grant number DGE-0654431 and the California NanoSystems Institute. C.N. acknowledges support from the NSF (grant # CMMI-1200547). The authors acknowledge the use of instruments at the Electron Imaging Center for NanoMachines supported by NIH (1S10RR23057) and CNSI at UCLA.

■ REFERENCES

(1) Jackson, N. E.; Savoie, B. M.; Marks, T. J.; Chen, L. X.; Ratner, M. A. The Next Breakthrough for Organic Photovoltaics? *J. Phys. Chem. Lett.* **2015**, *6*, 77−84.

(2) Nelson, J. Polymer: Fullerene Bulk Heterojunction Solar Cells. *Mater. Today* **2011**, *14*, 462−470.

(3) Grätzel, M. The Light and Shade of Perovskite Solar Cells. *Nat. Mater.* **2014**, *13*, 838−842.

(4) Kim, H.-S.; Im, S. H.; Park, N.-G. Organolead Halide Perovskite: New Horizons in Solar Cell Research. *J. Phys. Chem. C* **2014**, *118*, 5615−5625.

(5) Hawks, S. A.; Deledalle, F.; Yao, J.; Rebois, D. G.; Li, G.; Nelson, J.; Yang, Y.; Kirchartz, T.; Durrant, J. R. Relating Recombination, Density of States, and Device Performance in an Efficient Polymer:-Fullerene Organic Solar Cell Blend. *Adv. Energy Mater.* **2013**, *3*, 1201−1209.

(6) Hawks, S. A.; Li, G.; Yang, Y.; Street, R. A. Band Tail Recombination in Polymer:Fullerene Organic Solar Cells. *J. Appl. Phys.* **2014**, *116*, 074503.

(7) Street, R. A.; Hawks, S. A.; Khlyabich, P. P.; Li, G.; Schwartz, B. J.; Thompson, B. C.; Yang, Y. Electronic Structure and Transition Energies in Polymer-Fullerene Bulk Heterojunctions. *J. Phys. Chem. C* **2014**, *118*, 21873−21883.

(8) Aguirre, J. C.; Arntsen, C.; Hernandez, S.; Huber, R.; Nardes, A. M.; Halim, M.; Kilbride, D.; Rubin, Y.; Tolbert, S. H.; Kopidakis, N.; Schwartz, B. J.; Neuhauser, D. Understanding Local and Macroscopic Electron Mobilities in the Fullerene Network of Conjugated Polymer-based Solar Cells: Time-Resolved Microwave Conductivity and Theory. *Adv. Funct. Mater.* **2014**, *24*, 784−792.

(9) Vandewal, K.; Albrecht, S.; Hoke, E. T.; Graham, K. R.; Widmer, J.; Douglas, J. D.; Schubert, M.; Mateker, W. R.; Bloking, J. T.; Burkhard, G. F.; Sellinger, A.; Fréchet, J. M. J.; Amassian, A.; Riede, M. K.; McGehee, M. D.; Neher, D.; Salleo, A. Efficient Charge Generation by Relaxed Charge-Transfer States at Organic Interfaces. *Nat. Mater.* **2013**, *13*, 63−68.

(10) Mei, A.; Li, X.; Liu, L.; Ku, Z.; Liu, T.; Rong, Y.; Xu, M.; Hu, M.; Chen, J.; Yang, Y.; Gratzel, M.; Han, H. A Hole-Conductor-Free, Fully Printable Mesoscopic Perovskite Solar Cell with High Stability. *Science* **2014**, *345*, 295−298.

(11) Tremolet De Villers, B.; Tassone, C. J.; Tolbert, S. H.; Schwartz, B. J. Improving the Reproducibility of P3HT:PCBM Solar Cells by Controlling the PCBM/Cathode Interface. *J. Phys. Chem. C* **2009**, *113*, 18978−18982.

(12) Finck, B. Y.; Schwartz, B. J. Understanding the Origin of the S-Curve in Conjugated Polymer/Fullerene Photovoltaics from Drift-Diffusion Simulations. *Appl. Phys. Lett.* **2013**, *103*, 053306.

(13) Campoy-Quiles, M.; Ferenczi, T.; Agostinelli, T.; Etchegoin, P. G.; Kim, Y.; Anthopoulos, T. D.; Stavrinou, P. N.; Bradley, D. D. C.; Nelson, J. Morphology Evolution via Self-Organization and Lateral and Vertical Diffusion in Polymer: Fullerene Solar Cell Blends. *Nat. Mater.* **2008**, *7*, 158−164.

(14) Liu, Y.; Liu, F.; Wang, H. W. H.-W.; Nordlund, D.; Sun, Z.; Ferdous, S.; Russell, T. P. Sequential Deposition: Optimization of Solvent Swelling for High-Performance Polymer Solar Cells. *ACS Appl. Mater. Interfaces* **2015**, *7*, 653−661.

(15) Yu, Z.; Sun, L. Recent Progress on Hole-Transporting Materials for Emerging Organometal Halide Perovskite Solar Cells. *Adv. Energy Mater.* **2015**, *5*, 1500213.

(16) Wetzelaer, G.-J. A. H.; Scheepers, M.; Sempere, A. M.; Momblona, C.; Ávila, J.; Bolink, H. J. Trap-Assisted Non-Radiative Recombination in Organic-Inorganic Perovskite Solar Cells. *Adv. Mater.* **2015**, *27*, 1837−1841.

(17) Zhang, Y.; Liu, M.; Eperon, G. E.; Leijtens, T. C.; McMeekin, D.; Saliba, M.; Zhang, W.; de Bastiani, M.; Petrozza, A.; Herz, L. M.; Johnston, M. B.; Lin, H.; Snaith, H. J. Charge Selective Contacts, Mobile Ions and Anomalous Hysteresis in Organic-Inorganic Perovskite Solar Cells. *Mater. Horiz.* **2015**, *2*, 315−322.

(18) Ratcliff, E. L.; Garcia, A.; Paniagua, S. A.; Cowan, S. R.; Giordano, A. J.; Ginley, D. S.; Marder, S. R.; Berry, J. J.; Olson, D. C. Investigating the Influence of Interfacial Contact Properties on Open Circuit Voltages in Organic Photovoltaic Performance: Work Function Versus Selectivity. *Adv. Energy Mater.* **2013**, *3*, 647−656.

(19) Heo, J. H.; Im, S. H.; Noh, J. H.; Mandal, T. N.; Lim, C.-S.; Chang, J. A.; Lee, Y. H.; Kim, H.-j.; Sarkar, A.; Nazeeruddin, Md. K.; Gratzel, M.; Seok, S. I. Efficient Inorganic-Organic Hybrid Heterojunction Solar Cells Containing Perovskite Compound and Polymeric Hole Conductors. *Nat. Photonics* **2013**, *7*, 486−491.

(20) Jeon, N. J.; Noh, J. H.; Yang, W. S.; Kim, Y. C.; Ryu, S.; Seo, J.; Seok, S. I. Compositional Engineering of Perovskite Materials for High-Performance Solar Cells. *Nature* **2015**, *517*, 476−480.

(21) Chen, D.; Nakahara, A.; Wei, D.; Nordlund, D.; Russell, T. P. P3HT/PCBM Bulk Heterojunction Organic Photovoltaics: Correlating Efficiency and Morphology. *Nano Lett.* **2011**, *11*, 561−567.

(22) Seok, J.; Shin, T. J.; Park, S.; Cho, C.; Lee, J.-Y.; Yeol Ryu, D.; Kim, M. H.; Kim, K. Efficient Organic Photovoltaics Utilizing Nanoscale Heterojunctions in Sequentially Deposited Polymer/fullerene Bilayer. *Sci. Rep.* **2015**, *5*, 8373.

(23) Roehling, J. D.; Rochester, C. W.; Ro, H. W.; Wang, P.; Majewski, J.; Batenburg, K. J.; Arslan, I.; Delongchamp, D. M.; Moulé, A. J. Material Profile Influences in Bulk-Heterojunctions. *J. Polym. Sci., Part B: Polym. Phys.* **2014**, *52*, 1291−1300.

DOI: 10.1021/acsami.5b06944
ACS Appl. Mater. Interfaces 2015, 7, 25247−25258

(24) Mauger, S. A.; Chang, L.; Friedrich, S.; Rochester, C. W.; Huang, D. M.; Wang, P.; Moulé, A. J. Self-Assembly of Selective Interfaces in Organic Photovoltaics. *Adv. Funct. Mater.* **2013**, *23*, 1935−1946.
(25) Tseng, W.-H.; Lo, H.; Chang, J.-K.; Liu, I.-H.; Chen, M.-H.; Wu, C.-I. Metal-Induced Molecular Diffusion in [6,6]-Phenyl-C61-Butyric Acid Methyl Ester Poly(3-hexylthiophene) Based Bulk-Heterojunction Solar Cells. *Appl. Phys. Lett.* **2013**, *103*, 183506.
(26) Wertheim, G. K.; Buchanan, D. N. E. Reaction of C60 with Metals: W. *Solid State Commun.* **1993**, *88*, 97−100.
(27) Chikamatsu, M.; Taima, T.; Yoshida, Y.; Saito, K.; Yase, K. Mg-Doped C60 Thin Film as Improved N-Type Organic Semiconductor for A Solar Cell. *Appl. Phys. Lett.* **2004**, *84*, 127−129.
(28) Wang, H.; Hou, J. G.; Takeuchi, O.; Fujisuku, Y.; Kawazu, A. STM Observations of Ag-Induced Reconstruction of C60 Thin Films. *Phys. Rev. B: Condens. Matter Mater. Phys.* **2000**, *61*, 2199−2203.
(29) Devenyi, A.; Manaila, R.; Belu-Marian, A. Nanocrystalline Gold in Au-Doped Thin C60 Films. *Thin Solid Films* **1998**, *335*, 258−265.
(30) Matz, D. L.; Ratcliff, E. L.; Meyer, J.; Kahn, A.; Pemberton, J. E. Deciphering the Metal-C60 Interface in Optoelectronic Devices: Evidence for C60 Reduction by Vapor Deposited Al. *ACS Appl. Mater. Interfaces* **2013**, *5*, 6001−6008.
(31) Shukla, M. K.; Dubey, M.; Leszczynski, J. Theoretical Investigation of Electronic Structures and Properties of C60-Gold Nanocontacts. *ACS Nano* **2008**, *2*, 227−234.
(32) Tondelier, D.; Lmimouni, K.; Vuillaume, D.; Fery, C.; Haas, G. Metal/Organic/Metal Bistable Memory Devices. *Appl. Phys. Lett.* **2004**, *85*, 5763−5765.
(33) Scharnberg, M.; Adelung, R.; Faupel, F. Influence of Top Layer Geometries on the Electronic Properties of Pentacene and Diindenoperylene Thin Films. *Phys. Status Solidi A* **2008**, *205*, 578−590.
(34) Zhang, X. H.; Domercq, B.; Kippelen, B. Effect of Au Deposition Rate on the Performance of Top-Contact Pentacene Organic Field-Effect Transistors. *Synth. Met.* **2009**, *159*, 2371−2374.
(35) Fladischer, S.; Neuhold, A.; Kraker, E.; Haber, T.; Lamprecht, B.; Salzmann, I.; Resel, R.; Grogger, W. Diffusion of Ag into Organic Semiconducting Materials: A Combined Analytical Study Using Transmission Electron Microscopy and X-Ray Reflectivity. *ACS Appl. Mater. Interfaces* **2012**, *4*, 5608−5612.
(36) Yu, S.; Santoro, G.; Sarkar, K.; Dicke, B.; Wessels, P.; Bommel, S.; Döhrmann, R.; Perlich, J.; Kuhlmann, M.; Metwalli, E.; Risch, J. F. H.; Schwartzkopf, M.; Drescher, M.; Müller-Buschbaum, P.; Roth, S. V. Formation of Al Nanostructures on Alq3: An In situ Grazing Incidence Small Angle X-Ray Scattering Study During Radio Frequency Sputter Deposition. *J. Phys. Chem. Lett.* **2013**, *4*, 3170−3175.
(37) Dürr, A. C.; Schreiber, F.; Kelsch, M.; Carstanjen, H. D.; Dosch, H.; Seeck, O. H. Morphology and Interdiffusion Behavior of Evaporated Metal Films on Crystalline Diindenoperylene Thin Films. *J. Appl. Phys.* **2003**, *93*, 5201−5209.
(38) Schwartzkopf, M.; Santoro, G.; Brett, C. J.; Rothkirch, A.; Polonskyi, O.; Hinz, A.; Metwalli, E.; Yao, Y.; Strunskus, T.; Faupel, F.; Müller-Buschbaum, P.; Roth, S. V. Real-Time Monitoring of Morphology and Optical Properties during Sputter Deposition for Tailoring Metal-Polymer Interfaces. *ACS Appl. Mater. Interfaces* **2015**, *7*, 13547−13556.
(39) Kirchartz, T.; Agostinelli, T.; Campoy-Quiles, M.; Gong, W.; Nelson, J. Understanding the Thickness-Dependent Performance of Organic Bulk Heterojunction Solar Cells: The Influence of Mobility, Lifetime, and Space Charge. *J. Phys. Chem. Lett.* **2012**, *3*, 3470−3475.
(40) Hawks, S. A.; Finck, B. Y.; Schwartz, B. J. Theory of Current Transients in Planar Semiconductor Devices: Insights and Applications to Organic Solar Cells. *Phys. Rev. Appl.* **2015**, *3*, 44014.
(41) Natali, D.; Caironi, M. Charge Injection in Solution-Processed Organic Field-Effect Transistors: Physics, Models and Characterization Methods. *Adv. Mater.* **2012**, *24*, 1357−1387.
(42) Dongaonkar, S.; Servaites, J. D.; Ford, G. M.; Loser, S.; Moore, J.; Gelfand, R. M.; Mohseni, H.; Hillhouse, H. W.; Agrawal, R.; Ratner, M. a.; Marks, T. J.; Lundstrom, M. S.; Alam, M. A. Universality of Non-Ohmic Shunt Leakage in Thin-Film Solar Cells. *J. Appl. Phys.* **2010**, *108*, 124509.
(43) Wagner, J.; Gruber, M.; Wilke, A.; Tanaka, Y.; Topczak, K.; Steindamm, A.; Hörmann, U.; Opitz, A.; Nakayama, Y.; Ishii, H.; Pflaum, J.; Koch, N.; Brütting, W. Identification of Different Origins for S-Shaped Current Voltage Characteristics in Planar Heterojunction Organic Solar Cells. *J. Appl. Phys.* **2012**, *111*, 054509.
(44) Steindamm, A.; Brendel, M.; Topczak, a. K.; Pflaum, J. Thickness Dependent Effects of An Intermediate Molecular Blocking Layer on the Optoelectronic Characteristics of Organic Bilayer Photovoltaic Cells. *Appl. Phys. Lett.* **2012**, *101*, 143302.
(45) Dibb, G. F. A.; Muth, M.-A.; Kirchartz, T.; Engmann, S.; Hoppe, H.; Gobsch, G.; Thelakkat, M.; Blouin, N.; Tierney, S.; Carrasco-Orozco, M.; Durrant, J. R.; Nelson, J. Influence of Doping on Charge Carrier Collection in Normal and Inverted Geometry Polymer:-Fullerene Solar Cells. *Sci. Rep.* **2013**, *3*, 1−7.
(46) Bisquert, J.; Kirchartz, T.; Mora-Seró, I.; Garcia-Belmonte, G. Classification of Solar Cells According to Mechanisms of Charge Separation and Charge Collection. *Phys. Chem. Chem. Phys.* **2015**, *17*, 4007−4014.
(47) Reese, M. O.; White, M. S.; Rumbles, G.; Ginley, D. S.; Shaheen, S. E. Optimal Negative Electrodes for Poly(3-Hexylthiophene): 6,6-Phenyl C61-Butyric Acid Methyl Ester Bulk Heterojunction Photovoltaic Devices. *Appl. Phys. Lett.* **2008**, *92*, 053307.
(48) Amarandei, G.; Clancy, I.; Arshak, A.; Corcoran, D. Stability of Ultrathin Nanocomposite Polymer Films Controlled by the Embedding of Gold Nanoparticles. *ACS Appl. Mater. Interfaces* **2014**, *6*, 20758−20767.
(49) Chen, H.; Hsiao, Y.-C.; Hu, B.; Dadmun, M. Control of Morphology and Function of Low Band Gap Polymer-Bis-Fullerene Mixed Heterojunctions in Organic Photovoltaics with Selective Solvent Vapor Annealing. *J. Mater. Chem. A* **2014**, *2*, 9883−9890.
(50) Huang, J.-H.; Hsiao, Y.-S.; Richard, E.; Chen, C.-C.; Chen, P.; Li, G.; Chu, C.-W.; Yang, Y. The Investigation of Donor-Acceptor Compatibility in Bulk-Heterojunction Polymer Systems. *Appl. Phys. Lett.* **2013**, *103*, 043304.
(51) Parnell, A. J.; Dunbar, A. D. F.; Pearson, A. J.; Staniec, P. A.; Dennison, A. J. C.; Hamamatsu, H.; Skoda, M. W. A.; Lidzey, D. G.; Jones, R. A. L. Depletion of PCBM at the Cathode Interface in P3HT/PCBM Thin Films as Quantified via Neutron Reflectivity Measurements. *Adv. Mater.* **2010**, *22*, 2444−2447.
(52) Ayzner, A. L.; Tassone, C. J.; Tolbert, S. H.; Schwartz, B. J. Reappraising the Need for Bulk Heterojunctions in Polymer-Fullerene Photovoltaics: The Role of Carrier Transport in All-Solution-Processed P3HT/PCBM Bilayer Solar Cells. *J. Phys. Chem. C* **2009**, *113*, 20050−20060.
(53) Hawks, S. A.; Aguirre, J. C.; Schelhas, L. T.; Thompson, R. J.; Huber, R. C.; Ferreira, A. S.; Zhang, G.; Herzing, A. A.; Tolbert, S. H.; Schwartz, B. J. Comparing Matched Polymer:Fullerene Solar Cells Made by Solution-Sequential Processing and Traditional Blend Casting: Nanoscale Structure and Device Performance. *J. Phys. Chem. C* **2014**, *118*, 17413−17425.
(54) Zhang, G.; Huber, R. C.; Ferreira, A. S.; Boyd, S. D.; Luscombe, C. K.; Tolbert, S. H.; Schwartz, B. J. Crystallinity Effects in Sequentially Processed and Blend-Cast Bulk-Heterojunction Polymer/Fullerene Photovoltaics. *J. Phys. Chem. C* **2014**, *118*, 18424−18435.
(55) Aguirre, J. C.; Hawks, S. A.; Ferreira, A. S.; Yee, P.; Subramaniyan, S.; Jenekhe, S. A.; Tolbert, S. H.; Schwartz, B. J. Sequential Processing for Organic Photovoltaics: Design Rules for Morphology Control by Tailored Semi-Orthogonal Solvent Blends. *Adv. Energy Mater.* **2015**, *5*, 1402020.
(56) Lee, K. H.; Schwenn, P. E.; Smith, A. R. G.; Cavaye, H.; Shaw, P. E.; James, M.; Krueger, K. B.; Gentle, I. R.; Meredith, P.; Burn, P. L. Morphology of All-Solution-Processed "Bilayer" Organic Solar Cells. *Adv. Mater.* **2011**, *23*, 766−770.
(57) Lee, K. H.; Zhang, Y.; Burn, P. L.; Gentle, I. R.; James, M.; Nelson, A.; Meredith, P. Correlation of Diffusion and Performance in

DOI: 10.1021/acsami.5b06944
ACS Appl. Mater. Interfaces 2015, 7, 25247−25258

Sequentially Processed P3HT/PCBM Heterojunction Films by Time-Resolved Neutron Reflectometry. *J. Mater. Chem. C* **2013**, *1*, 2593−2598.
(58) Tomita, Y.; Nakayama, T. In *Electron. Process. Org. Electron.*; Ishii, H., Kudo, K., Nakayama, T., Ueno, N., Eds.; Springer Series in Materials Science; Springer Japan: Tokyo, 2015; Chapter 14, pp 303−317.
(59) Tomita, Y.; Nakayama, T. Metal-Atom Diffusion in Organic Solids: First-Principles Study of Graphene and Polyacetylene Systems. *Appl. Phys. Express* **2010**, *3*, 091601.
(60) Abrusci, A.; Stranks, S. D.; Docampo, P.; Yip, H.-L.; Jen, A. K.-Y.; Snaith, H. J. High-Performance Perovskite-Polymer Hybrid Solar Cells via Electronic Coupling with Fullerene Monolayers. *Nano Lett.* **2013**, *13*, 3124−3128.
(61) Shao, Y.; Xiao, Z.; Bi, C.; Yuan, Y.; Huang, J. Origin and Elimination of Photocurrent Hysteresis by Fullerene Passivation in CH3NH3PbI3 Planar Heterojunction Solar Cells. *Nat. Commun.* **2014**, *5*, 5784.
(62) Jeng, J.-Y.; Chiang, Y.-F.; Lee, M.-H.; Peng, S.-R.; Guo, T.-F.; Chen, P.; Wen, T.-C. CH3NH3PbI3 Perovskite/Fullerene Planar-Heterojunction Hybrid Solar Cells. *Adv. Mater.* **2013**, *25*, 3727−3732.
(63) Ayzner, A. L.; Wanger, D. D.; Tassone, C. J.; Tolbert, S. H.; Schwartz, B. J. Room to Improve Conjugated Polymer-Based Solar Cells: Understanding How Thermal Annealing Affects the Fullerene Component of a Bulk Heterojunction Photovoltaic Device. *J. Phys. Chem. C* **2008**, *112*, 18711−18716.
(64) Beek, W. J. E.; Wienk, M. M.; Kemerink, M.; Yang, X.; Janssen, R. A. J. Hybrid Zinc Oxide Conjugated Polymer Bulk Heterojunction Solar Cells. *J. Phys. Chem. B* **2005**, *109*, 9505−9516.
(65) Takacs, C. J.; Treat, N. D.; Krämer, S.; Chen, Z.; Facchetti, A.; Chabinyc, M. L.; Heeger, A. J. Remarkable Order of A High-Performance Polymer. *Nano Lett.* **2013**, *13*, 2522−2527.
(66) Egerton, R. F.; Li, P.; Malac, M. Radiation Damage in the TEM and SEM. *Micron* **2004**, *35*, 399−409.
(67) Herzing, A. A.; Ro, H. W.; Soles, C. L.; DeLongchamp, D. M. Visualization of Phase Evolution in Model Organic Photovoltaic Structures via Energy-Filtered Transmission Electron Microscopy. *ACS Nano* **2013**, *7*, 7937−7944.
(68) Cheng, P.; Hou, J.; Li, Y.; Zhan, X. Layer-by-Layer Solution-Processed Low-Bandgap Polymer-PC61BM Solar Cells with High Efficiency. *Adv. Energy Mater.* **2014**, *4*, 1301349.
(69) Juška, G.; Arlauskas, K.; Viliūnas, M. Charge Transport in π-Conjugated Polymers from Extraction Current Transients. *Phys. Rev. B: Condens. Matter Mater. Phys.* **2000**, *62*, 235−238.
(70) Bange, S.; Schubert, M.; Neher, D. Charge Mobility Determination by Current Extraction under Linear Increasing Voltages: Case of Nonequilibrium Charges and Field-Dependent Mobilities. *Phys. Rev. B: Condens. Matter Mater. Phys.* **2010**, *81*, 35209.
(71) Sandberg, O. J.; Nyman, M.; Österbacka, R. Direct Determination of Doping Concentration and Built-in Voltage from Extraction Current Transients. *Org. Electron.* **2014**, *15*, 3413−3420.
(72) Armin, A.; Juška, G.; Philippa, B. W.; Burn, P. L.; Meredith, P.; White, R. D.; Pivrikas, A. Doping-Induced Screening of the Built-in-Field in Organic Solar Cells: Effect on Charge Transport and Recombination. *Adv. Energy Mater.* **2013**, *3*, 321−327.
(73) van Franeker, J. J.; Kouijzer, S.; Lou, X.; Turbiez, M.; Wienk, M. M.; Janssen, R. A. J. Depositing Fullerenes in Swollen Polymer Layers via Sequential Processing of Organic Solar Cells. *Adv. Energy Mater.* **2015**, *5*, 1500464.
(74) Rochester, C. W.; Mauger, S. A.; Moule, A. J. Investigating the Morphology of Polymer/Fullerene Layers Coated Using Orthogonal Solvents. *J. Phys. Chem. C* **2012**, *116*, 7287−7292.
(75) Liu, T.; Troisi, A. Absolute Rate of Charge Separation and Recombination in a Molecular Model of the P3HT/PCBM Interface. *J. Phys. Chem. C* **2011**, *115*, 2406−2415.
(76) Taylor, J. R. *An Introduction to Error Analysis, the Study of Uncertainties in Physical Measurements*, 2nd ed.;University Science Books: Sausalito, CA, 1997.
(77) Gupta, D. *Diffusion Processes in Advanced Technological Materials*; William Andrew, Inc.: Norwich, NY, 2005; Chapter 7, pp 333−363.
(78) Treat, N. D.; Brady, M. A.; Smith, G.; Toney, M. F.; Kramer, E. J.; Hawker, C. J.; Chabinyc, M. L. Interdiffusion of PCBM and P3HT Reveals Miscibility in a Photovoltaically Active Blend. *Adv. Energy Mater.* **2011**, *1*, 82−89.
(79) Li, G.; Chu, C. W.; Shrotriya, V.; Huang, J.; Yang, Y. Efficient Inverted Polymer Solar Cells. *Appl. Phys. Lett.* **2006**, *88*, 253503.
(80) You, J.; Chen, C.-C.; Dou, L.; Murase, S.; Duan, H.-S.; Hawks, S. A.; Xu, T.; Son, H. J.; Yu, L.; Li, G.; Yang, Y. Metal Oxide Nanoparticles as an Electron-Transport Layer in High-Performance and Stable Inverted Polymer Solar Cells. *Adv. Mater.* **2012**, *24*, 5267−5272.
(81) He, Z.; Zhong, C.; Su, S.; Xu, M.; Wu, H.; Cao, Y. Enhanced Power-Conversion Efficiency in Polymer Solar Cells Using an Inverted Device Structure. *Nat. Photonics* **2012**, *6*, 593−597.
(82) Zhao, G.; He, Y.; Li, Y. 6.5% Efficiency of Polymer Solar Cells Based on Poly(3-Hexylthiophene) and Indene-C(60) Bisadduct by Device Optimization. *Adv. Mater.* **2010**, *22*, 4355−4358.
(83) He, Y.; Chen, H. Y.; Hou, J.; Li, Y. Indene-C60 Bisadduct: A New Acceptor for High-Performance Polymer Solar Cells. *J. Am. Chem. Soc.* **2010**, *132*, 1377−1382.
(84) Steuerman, D. W.; Garcia, a.; Dante, M.; Yang, R.; Löfvander, J. P.; Nguyen, T.-Q. Imaging the Interfaces of Conjugated Polymer Optoelectronic Devices. *Adv. Mater.* **2008**, *20*, 528−534.
(85) Wang, D. H.; Moon, J. S.; Seifter, J.; Jo, J.; Park, J. H.; Park, O. O.; Heeger, A. J. Sequential Processing: Control of Nanomorphology in Bulk Heterojunction Solar Cells. *Nano Lett.* **2011**, *11*, 3163−3168.
(86) Sun, Y.; Welch, G. C.; Leong, W. L.; Takacs, C. J.; Bazan, G. C.; Heeger, A. J. Solution-Processed Small-Molecule Solar Cells with 6.7% Efficiency. *Nat. Mater.* **2011**, *11*, 44−48.
(87) Machui, F.; Rathgeber, S.; Li, N.; Ameri, T.; Brabec, C. J. Influence of a Ternary Donor Material on the Morphology of a P3HT:PCBM Blend for Organic Photovoltaic Devices. *J. Mater. Chem.* **2012**, *22*, 15570−15577.
(88) Bebensee, F.; Schmid, M.; Steinrück, H.-P.; Campbell, C. T.; Gottfried, J. M. Toward Well-Defined Metal-Polymer Interfaces: Temperature-Controlled Suppression of Subsurface Diffusion and Reaction at the Calcium/Poly(3-hexylthiophene) Interface. *J. Am. Chem. Soc.* **2010**, *132*, 12163−12165.
(89) Bebensee, F.; Zhu, J.; Baricuatro, J. H.; Farmer, J. A.; Bai, Y.; Steinrück, H.-P.; Campbell, C. T.; Gottfried, J. M. Interface Formation between Calcium and Electron-Irradiated Poly(3-hexylthiophene). *Langmuir* **2010**, *26*, 9632−9639.
(90) Atwater, H. A.; Polman, A. Plasmonics for Improved Photovoltaic Devices. *Nat. Mater.* **2010**, *9*, 205−213.
(91) Gan, Q.; Bartoli, F. J.; Kafafi, Z. H. Plasmonic-Enhanced Organic Photovoltaics: Breaking the 10% Efficiency Barrier. *Adv. Mater.* **2013**, *25*, 2385−2396.
(92) Xue, M.; Li, L.; Tremolet De Villers, B. J.; Shen, H.; Zhu, J.; Yu, Z.; Stieg, A. Z.; Pei, Q.; Schwartz, B. J.; Wang, K. L. Charge-Carrier Dynamics in Hybrid Plasmonic Organic Solar Cells with Ag Nanoparticles. *Appl. Phys. Lett.* **2011**, *98*, 253302.
(93) Ahn, S.; Jang, W.; Park, J. H.; Wang, D. H. Enhanced Performance of Layer-Evolved Bulk-Heterojunction Solar Cells with Ag Nanoparticles by Sequential Deposition. *Org. Electron.* **2015**, *24*, 325−329.
(94) Burkhard, G. F.; Hoke, E. T.; McGehee, M. D. Accounting for Interference, Scattering, and Electrode Absorption to Make Accurate Internal Quantum Efficiency Measurements in Organic and Other Thin Solar Cells. *Adv. Mater.* **2010**, *22*, 3293−3297.
(95) Peumans, P.; Yakimov, A.; Forrest, S. R. Small Molecular Weight Organic Thin-Film Photodetectors and Solar Cells. *J. Appl. Phys.* **2003**, *93*, 3693−3723.
(96) Ghosh, S. K.; Pal, T. Interparticle Coupling Effect on the Surface Plasmon Resonance of Gold Nanoparticles: From Theory to Applications. *Chem. Rev.* **2007**, *107*, 4797−4862.

DOI: 10.1021/acsami.5b06944
ACS Appl. Mater. Interfaces 2015, 7, 25247−25258

(97) Geng, M.; Zhang, Y.; Huang, Q.; Zhang, B.; Li, Q.; Li, W.; Li, J. Functionalization of C60 with Gold Nanoparticles. *Carbon* **2010**, *48*, 3570−3574.
(98) Yip, H.-L.; Jen, A. K.-Y. Recent Advances in Solution-Processed Interfacial Materials for Efficient and Stable Polymer Solar Cells. *Energy Environ. Sci.* **2012**, *5*, 5994−6011.

DOI: 10.1021/acsami.5b06944
ACS Appl. Mater. Interfaces 2015, 7, 25247−25258